Kashani MN, Zivkovic V, Elekaei H, Herrera LF, Affleck K, Biggs MJ.

A new method for reconstruction of the structure of micro-packed beds of spherical particles from desktop X-ray microtomography images. Part B. Structure refinement and analysis.

***Chemical Engineering Science* (2016)**

DOI: 10.1016/j.ces.2016.05.036

A new method for reconstruction of the structure of micro-packed beds of spherical particles from desktop X-ray microtomography images. Part B. Structure refinement and analysis

M. Navvab Kashani,[1] V. Zivkovic,[2] H. Elekaei,[1] L.F. Herrera,[3] K. Affleck,[1] M.J. Biggs[1,4,*]

1. School of Chemical Engineering, The University of Adelaide, SA 5005, Australia.
2. School of Chemical Engineering and Advanced Materials, Newcastle University, Merz Court, Newcastle-upon-Tyne, NE1 7RU, UK.
3. School of Engineering and Information Technology, Charles Darwin University, NT 0909, Australia.
4. School of Science, Loughborough University, Loughborough, LE11 3TU, UK.

Abstract

The authors have reported elsewhere (*Chem. Eng. Sci.*, **146**, 337, 2016) a new method that derives models of micro-packed beds (μPBs) of near-spherical particles from X-ray microtomography grayscale images of limited resolution compared to the characteristics dimensions of the particles and porosity. The new method is distinguished by it not requiring a grayscale threshold to partition the images into solid and void phases, and its retention of the underlying spherical geometry, two issues that are particularly problematic when more traditional approaches are used to build models of μPBs. Here it is shown that a reverse Monte Carlo (RMC) algorithm combined with simulated annealing (SA) can refine the models obtained from this new method to eliminate the vast majority of particle overlaps and incorporate particle size distributions. Application of the RMC-SA to an initial model of a μPB yielded a porosity estimate that was, within experimental uncertainty, the same as its directly measured counterpart. It was further shown that the porosity of μPBs is near unity at the bed wall and oscillates in a decaying fashion normal to the wall up to a distance of around three particle diameters into the bed. This leads to the porosity decreasing with increasing bed-to-particle diameter ratio. The opposite was observed, however, for the average number of particle-particle contacts (the mean coordination number). This latter behaviour has two origins: one in which the bulk of the bed where the coordination number is maximal and constant exerts increasing influence (volumetric origin), and one in which the packing density inherently decreases with the bed-to-particle diameter ratio (packing origin).

Keywords: Microfluidics; micro-packed bed (μPB); porosity; mean coordination number; wall effect; Reverse Monte-Carlo and simulated annealing.

* m.biggs@lboro.ac.uk

1. Introduction

Packings of near-spherical particles of 10s of microns diameter or smaller within channels of a few 100s of microns or less are commonly used in microfluidic applications ranging from microanalysis [1-5] through to process intensification [6-9]. Understanding the variation of the three-dimensional (3D) structure of such micro-packed beds (µPBs) as a function of the material characteristics and preparation conditions is critical to optimizing their performance [10]. As summarized in the first part of this contribution [11], hereafter referred to as Part A, there are a variety of experimental methods available for imaging the 3D structure of µPBs, but one of the most convenient is benchtop X-ray microtomography due to its modest cost and ease of use. However, its limited resolution relative to the porosity and particles in µPBs presents significant challenges when seeking to transform microtomography images of such beds into 3D models suitable for detailed quantitative analysis [11]. The first challenge is the identification of an appropriate threshold for turning the grayscale images obtained from X-ray microtomography such as that shown in Figure 1(a) into a binary image of solid and void only as shown in Figure 1(b) and (c). The second challenge is the loss of the underlying spherical geometry as also clearly demonstrated in Figure 1.

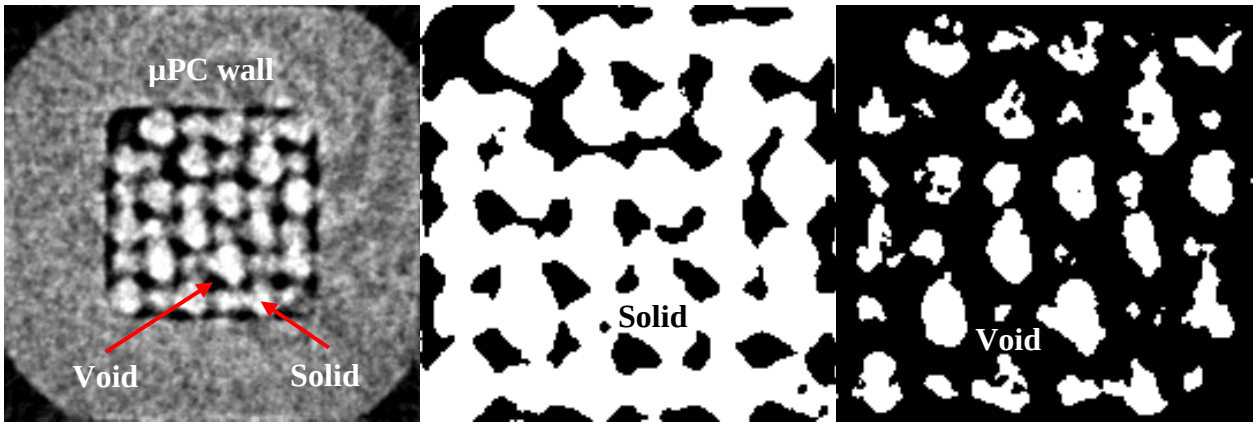

(a) (b) (c)

Figure 1. X-ray microtomography related images of a cross-section through a µPB composed of 38.5 µm diameter particles of high sphericity within a 200 µm square capillary: (a) raw grayscale image; (b) a binarized version of the greyscale image using a threshold of 60% of the grayscale range; and (c) a binarized version of the greyscale image using a threshold identified by the Otsu [12] method (80% of the grayscale range).

In Part A, we have outlined a method for converting benchtop X-ray microtomography grayscale images for µPBs into 3D models of sphere packings that does not rely on the identification of a grayscale threshold for partitioning the pixels between the solid and void phases. It was shown that this new method can yield a model of a µPB whose porosity is, within experimental error, equal to

the directly measured counterpart. The models obtained by the method outlined in Part A are, however, imperfect in that they include particles that overlap each other and the channel walls and particles that have no contact with any supporting particles (*i.e.* they are suspended). This reflects the fact that the method for identifying the particle positions is subject to some uncertainty and the particle sizes are all assumed equal to the experimentally determined mean (*i.e.* the particle sizes are not distributed as would be the case in reality). Here we detail the use of a Reverse Monte Carlo (RMC) simulation [13] combined with Simulated Annealing (SA) [14] to refine the structure obtained by the method described in Part A to address these two issues. The approach is first described and then demonstrated by using it to determine the porosity and topology of μPBs of near-spherical particles as a function of the particle-to-bed diameter.

2. Description of the new method

In order to eliminate particle-particle and particle-wall overlaps and suspended particles, Reverse Monte Carlo (RMC) was combined with Simulated Annealing (SA) to shift the particle size distribution (PSD) towards the experimentally-determined distribution and move the particle positions within the confines of their uncertainty. This involved repeatedly applying with equal probability the following two types of 'moves' to randomly selected spheres in the model derived from the method described in Part A:

1. **Changing the size of the particle** by an amount δd within the constraints of the experimental PSD

$$\delta d = \delta d_{max}(\xi - 0.5) \tag{1}$$

where $\delta d_{\max}$ is the maximum possible change in the diameter allowed and ξ is a random number selected in a uniform way from the range [0,1).

2. **Displacing the position of the sphere** in the three coordinate directions by δx_α within the degree of uncertainty associated with the estimated positions of the sphere centroid

$$\delta x_\alpha = \delta x_{\alpha,max}(\xi_\alpha - 0.5) \tag{2}$$

where $\delta x_{\alpha,max}$ is the maximum possible displacement allowed in the α-coordinate direction, and ξ_α are corresponding random numbers independently selected in a uniform way from the range [0,1).

The maximum particle diameter change and displacement allowed were adapted so as to yield a move acceptance ratio (the ratio of accepted moves to total attempted moves) of between 30 and 50%.

Each attempt at a move was accepted provided a random number selected uniformly from the range [0,1) was less than the probability [15]

$$P = \min(1,\ \exp[-\Delta F/T]) \tag{3}$$

where ΔF is the change the move would create in the functional we are seeking to minimise if accepted, and T is a 'temperature' that decreases monotonically during the course of the simulation; the cooling rate over two successive steps of $T(s)/T(s-1) = 0.9$ was used in the work reported here; although this 'cooling rate' was found to be satisfactory, other values can be used and, indeed, may be better from the perspective of computational efficiency (*i.e.* achieving a steady state value of the functional to be minimised, F) or accuracy (*i.e.* achieving the smallest possible value of F). Equation (3) ensures the move is always accepted if it brings a decrease or no change in the functional (*i.e.* $\Delta F \leq 0$) whilst allowing for it to also be accepted with a probability less than unity if the functional will increase with the move (*i.e.* $\Delta F > 0$). The use of the monotonically decreasing 'temperature' means the chances of such an 'uphill step' in F being accepted decreases from a maximum at the start of a simulation, all else being equal.

The functional that was minimized is

$$F = W_{pp}F_{pp} + W_{pw}F_{pw} + W_pF_p + W_sF_s \tag{4}$$

where the F_i and W_i are sub-functionals and associated weights, respectively, that relate to the differences that must be minimised in the simulation. The first term in this equation seeks to eliminate the particle-particle overlaps within the bed

$$F_{pp} = \sum_{ij}\left(\frac{D_{ij}}{d_{ij}}\right)^2 \tag{5}$$

where the summation is over all particle pairs, and D_{ij} is their overlap given by

$$D_{ij} = \begin{cases} \|\mathbf{x}_i - \mathbf{x}_j\| - d_{ij} & \text{if } \|\mathbf{x}_i - \mathbf{x}_j\| < d_{ij} \\ 0 & \text{if } \|\mathbf{x}_i - \mathbf{x}_j\| \geq d_{ij} \end{cases} \tag{6}$$

where $\mathbf{x}_i$ and $\mathbf{x}_j$ are the vectors defining the centroids of the particles-i and -j relative to an origin, and d_{ij} is the minimum distance that may exist between them in the absence of an overlap, which is given by the sum of the particle radii

$$d_{ij} = \frac{d_i + d_j}{2} \tag{7}$$

The second term in Equation (4) is similarly aimed at eliminating the particle overlaps with the confining walls of the µPB

$$F_{pw} = \sum_{iw} \left(\frac{D_{iw}}{d_i}\right)^2 \tag{8}$$

where the summation is over all particle-wall pairs, and D_{iw} is their overlap given by

$$D_{iw} = \begin{cases} (\hat{\mathbf{n}}_w \cdot \mathbf{x}_i + p_w) - d_{iw} & \text{if } (\hat{\mathbf{n}}_w \cdot \mathbf{x}_i + p_w) < d_{iw} \\ 0 & \text{if } (\hat{\mathbf{n}}_w \cdot \mathbf{x}_i + p_w) \geq d_{iw} \end{cases} \tag{9}$$

where $\hat{\mathbf{n}}_w$ is the unit normal to the wall-*w* and p_w its distance from the origin, and d_{iw} is the minimum distance that may exist between the particle and wall in the absence of an overlap, which is given by the particle radius

$$d_{iw} = \frac{d_i}{2} \tag{10}$$

The penultimate term in Equation (4), which is aimed at limiting the displacement of the particle centroids to within a region around their initial position commensurate with its uncertainty, is of the form

$$F_p = \sum_i D_{i0} \tag{11}$$

where the summation is over all particles, and D_{i0} is the amount the displacement of the particle from its initial position exceeds the uncertainty associated with the initial centroid position of the particle-*i*, which is given by

$$D_{i0} = \begin{cases} \|\mathbf{x}_i - \mathbf{x}_{i0}\| - \sigma_i & \text{if } \|\mathbf{x}_i - \mathbf{x}_{i0}\| > \sigma_i \\ 0 & \text{if } \|\mathbf{x}_i - \mathbf{x}_{i0}\| \leq \sigma_i \end{cases} \tag{12}$$

where $\mathbf{x}_{i0}$ is the position of the particle in the initial 3D structure obtained from the method described in Part A, and σ_i is the standard deviation associated with this position.

The final term in Equation (4) is aimed at minimising the difference between the experimental particle size distribution and that of the particle ensemble in the 3D model. It does this by considering the deviation between the mean, μ, standard deviation, σ, and skewness, κ, of the two distributions

$$F_s = \frac{(\mu_e - \mu_m)^2}{\mu_e^2} + \frac{(\sigma_e - \sigma_m)^2}{\sigma_e^2} + \frac{(\kappa_e - \kappa_m)^2}{\kappa_e^2} \tag{13}$$

where the subscripts *e* and *m* refer to the values from experiment and the model, respectively.

The weights for each term in Equation (4) are necessary to ensure the four terms are all of the same order. As the scale of each term varies during the simulation, the weights are varied during the simulation [16]. This was done by multiplying each weight by $\alpha \geq 1$ or $\beta \leq 1$ every N steps if their associated sub-functional was above or below the average of all the sub-functionals, respectively. Experimentation indicated that the scale of the sub-functionals could change relative to each other by up to 10% over 1000 MC steps and, thus, for the work reported here $N = 1000$ was used with $\alpha = 1.1$ and $\beta = 0.9$.

3. Application of the new method

The new approach was applied to models of μPBs constructed using the approach outlined in Part A. The materials were also essentially the same as in Part A except, as specified in Table 1, a wider range of particle and channel sizes were used to give a total of eight different bed-to-particle diameter ratios. The PSD for the 30.5 μm sized particles, which was determined using a Mastersizer 2000 (Malvern, UK) fitted with a Hydro 2000MU dispersion unit, is shown by way of example in Figure 1 with its standard deviation and skewness.

Table 1. Characteristics dimensions of the μPBs considered in the study reported here

Micro-capillary size*, D (μm)	Average particle diameter†, $\overline{d_p}$ (μm)	$D/\overline{d_p}$
200	38.5	5.2
200	34.5	5.8
200	30.5	6.6
200	26.5	7.6
400	38.5	10.4
400	34.5	11.6
400	30.5	13.2
400	26.5	15.2

* The micro-capillary cross-sections are square and they were filled to a depth of 50 mm.
† The standard deviation in the diameters of the soda-lime glass particles is 1.5 μm, and their sphericity 95%.

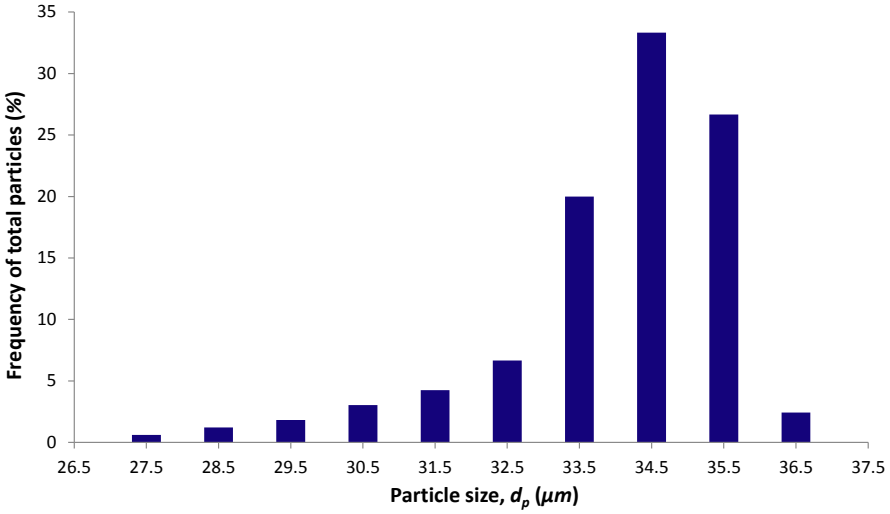

Figure 2. Particle size distribution (PSD) of the particles with an average diameter of 34.5 μm. The standard deviation and skewness are $\sigma_e = 1.51$ μm and $\kappa_e = -1.63$, respectively.

As in Part A, the images of the μPBs were acquired using A SkyScan1072 X-ray micro-CT system (SKYSCAN, Belgium). The reader is referred to Part A for the methodological details of the image acquisition.

4. Results and Discussion

Overview of initial interpretation of X-ray microtomography images of μPBs

Figure 3 shows examples of cross-sectional images from the eight different μPBs considered in the study reported here; see Figure 1(a) for how to interpret these greyscale images. These illustrate the challenges faced in imaging the particles and pore space. In particular, the degree to which one can discern the spherical geometry diminishes rapidly as the particle size decreases much below the largest within the smallest micro-channel (*i.e.* for$D/\overline{d_p} > 5.8$), and the boundary between the solid and void phases is not easily discerned.

By way of example, the transformation between Figure 4(a) and Figure 4(b) illustrates the outcome of application of the approach detailed in Part A to one of the cross-sectional images in the $D/\overline{d_p}$=5.2 μPB. As the circles with the red outlines highlight, some of the circular cross-sections extracted using the method of Part A lead to particle-particle and particle-wall overlaps. These can be removed by application of the methodology detailed in Section 2 above.

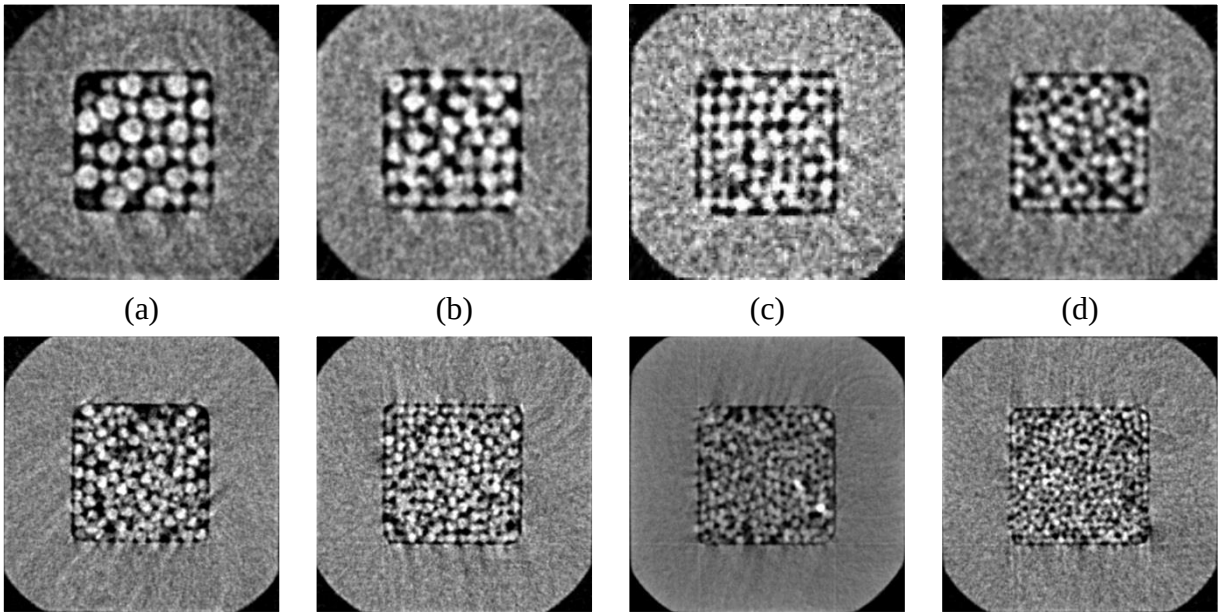

Figure 3. Example X-ray microtomography images of cross-sections of µPBs for bed-to-particle diameter ratios, $D/\overline{d_p}$, equal to (see Table 1 for more details): (a) 5.2; (b) 5.8; (c) 6.6; (d) 7.6; (e) 10.4; (f) 11.6; (g) 13.2; and (h) 15.2.

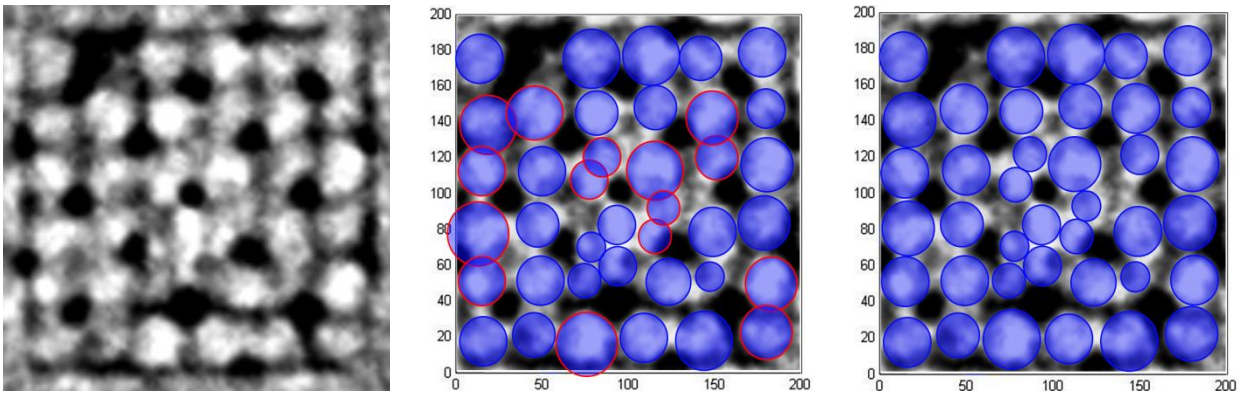

Figure 4. Example cross sections from key stages in the model construction: (a) a close-up of an X-ray microtomography image of a cross-section through the $D/\overline{d_p} = 5.2$ µPB; (b) the particle cross-sections identified through application of the methodology in Part A to the X-ray image, with the particles that are overlapping either each other or the walls shown with red outlines; and (c) the particle cross-sections shown in part (b) after application of the RMC-SA algorithm described herein to eliminate overlaps and obtain a PSD that is in line with the experimental one.

Structural change during an RMC-SA simulation

Figure 5(a) shows a typical variation of the objective function in Equation 4; the corresponding changes in the four parts that make up this objective function (not shown) are similar to what is seen here for the overall functional. The simulation in this example continued for approximately 1.3M steps before the objective function ceased to change. The values of the objective functions typically

dropped to between 1-10% of the initial value, indicating the ability of the approach to substantially eliminate overlaps and bring about a particle size distribution that matches the experimental one. These changes are illustrated in the transformation between Figure 4(b) and Figure 4(c), and in the shift in the character of the PSD as shown in Figure 5(b). The latter figure clearly shows that the PSD of the model broadens over the course of the simulation from its initial non-disperse character (black bar) to that seen experimentally (dotted bars *vs.* broken line).

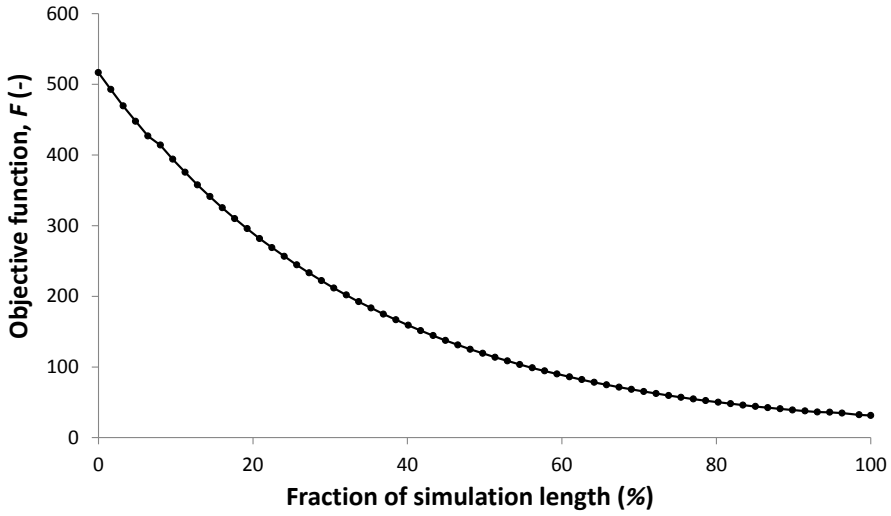

(a)

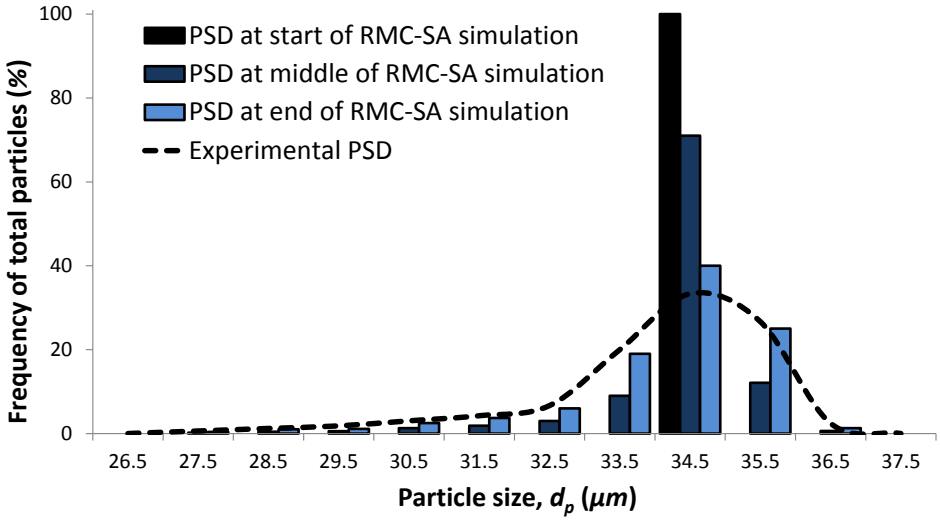

(b)

Figure 5. Variation of key structure-related metrics during a typical RMC-SA simulation: (a) objective function, *F*, (each point is an average over 100 steps); and (b) PSD (note the initial distribution is a single bar centred at 34.5 μm).

Qualitative analysis of packing structure in μPBs

Figure 6 shows a typical 3D model obtained from the application of the RMC-SA algorithm. The random nature of the packing is revealed in the various close-ups of the packing, particularly that shown in part (c). Part (e) of this figure shows the porosity is far more open near the bed wall, as anticipated. Interestingly, this part of the figure also shows that the model includes some particles that have no contacts with surrounding particles when located near the wall. Whilst this may reflect the RMC-SA algorithm is not entirely effective in removing non-physical occurrences, they were largely observed to occur near the wall, suggesting that surface forces between the particles and the capillary wall may be playing a role, something that has been observed in other systems, including micro-channels [17], porous media [18] and micro-fluidized beds that fail to fluidize due to the surface forces being more significant than the prevailing hydrodynamic forces [19, 20]. Comparison between the starting model (*i.e.* that obtained from the algorithm detailed in Part A) and that obtained after application of RMC-SA indicated more than 94% of the particle overlaps were eliminated. Of the few remaining, an example of which is seen in Figure 6(g), the degree of overlap was generally less than 1% (*i.e.* $D_{ij}/d_{ij} < 1\%$). Inspection of these defects in the model always revealed a situation where particle size and position adjustment would not remove the problem without compromising the functional, perhaps indicating that inclusion of non-spherical character may be of benefit (the sphericity of the particles was high, but not perfectly so).

Quantitative analysis of porosity in μPBs

Figure 7 shows the variation of the μPB porosity, determined *via* Monte Carlo integration on the reconstructed structures as described in Part A, with the bed-to-particle diameter ratio, in addition to data drawn from the literature and the value obtained *via* direct measurement for the $D/\overline{d_p} = 6.6$ μPB (see Part A for details of this measurement). The first thing to note is the porosity obtained from the reconstructed structure of the $D/\overline{d_p} = 6.6$ μPB, $53.6 \pm 1.4\%$, is statistically the same as that determined directly, $52 \pm 2\%$. This represents a further improvement on estimating the porosity compared to what was already a significant improvement gained in Part A, providing further reassurance that the model structures obtained using the algorithm described here are representative of the actual.

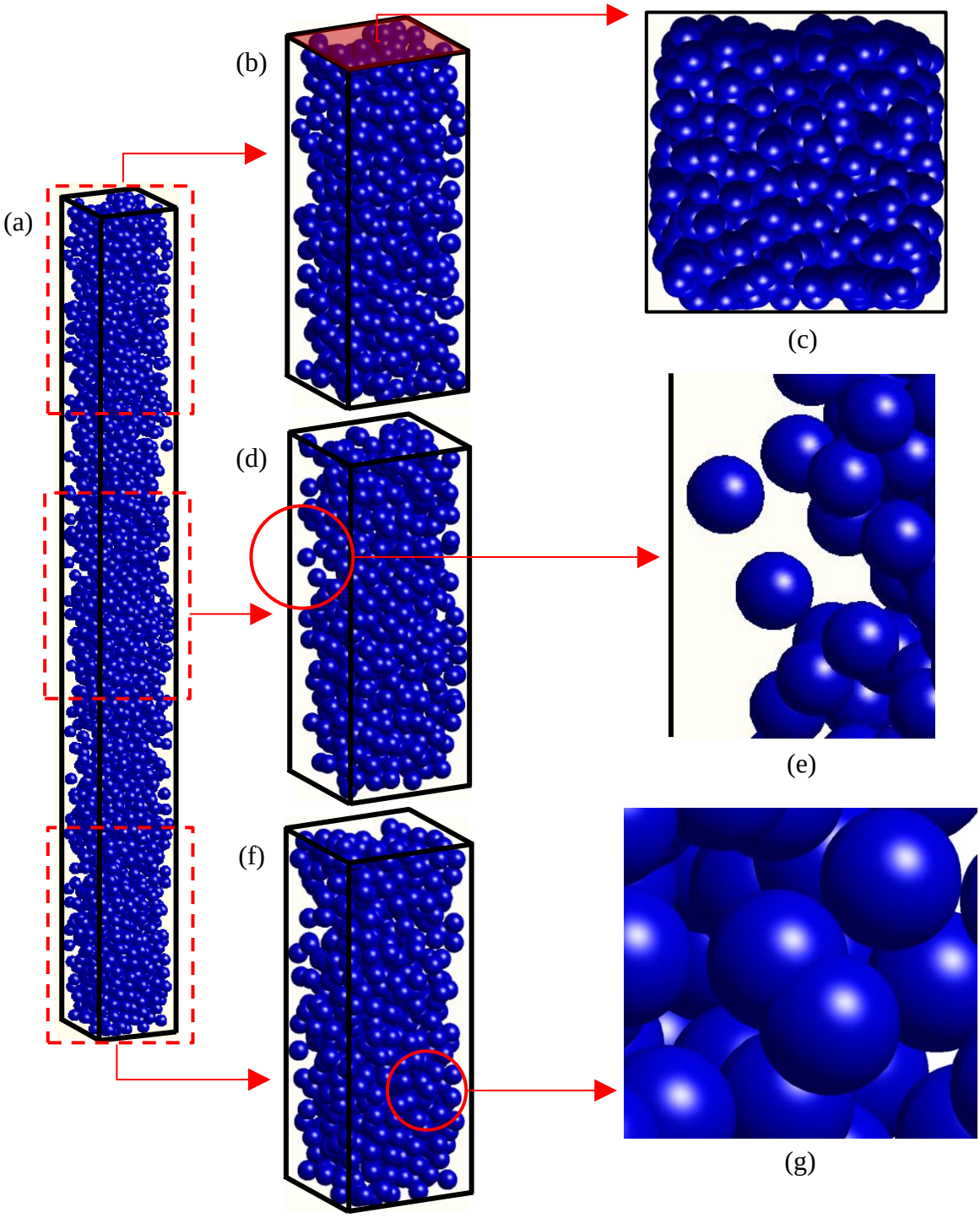

Figure 6. A model of the $D/\overline{d_p} = 5.2$ μPB shown from various perspectives: (a) complete bed; (b) a zoom on top third; (c) further zoom on top region of the bed to illustrate its random structure; (d) zoom on middle third; (e) further zoom on middle region of the bed to show the packing structure near the wall; (f) zoom on bottom third of the bed; and (g) further zoom on bottom region of the bed to show two particles that are still overlapping to some extent.

Figure 7(a) shows that the porosity of μPCs essentially decreases monotonically with bed-to-particle diameter ratio. This behaviour reflects the decreasing influence of the confining walls on the packing structure on a volumetric basis as suggested by the particle density maps shown in the Figure 8, which were derived by averaging the grey scale images obtained along the length of the μPB. The particles adjacent to the capillary walls are well ordered in all the μPBs, whilst the same can be said for the ring of particles sitting immediately adjacent to these outermost particles, although the ordering tends to diminish as the bed-to-particle diameter ratio increases. The particles within the two outer rings are well ordered for the three smaller beds, whilst little order exists for the larger μPBs.

This decreasing trend in Figure 7(a) is not dissimilar to that seen by De Klerk [21] for a macroscale PB of circular cross section. The overall porosities are higher here, however, due at least in part to the inaccessibility of the corners of the square cross-section of our μPBs as indicated by the broken line in Figure 7(b), which shows the porosity is near-unity for a distance of up to ~25% of the average particle diameter from the corner. Another potential origin of the differences seen between the two data sets is the sedimentation method used to create the μPBs here, which is likely to result in a much looser packing compared to that obtained in macroscale beds where gravity effects are proportionately more significant and tapping is more effective.

Figure 7(b) shows an example of the porosity variation normal to the walls; data for all the other beds are shown in the SI. This indicates that the local porosity varies in a damped-oscillatory manner for up to around three particle diameters into the bed before stabilising to a near-constant value. Following De Klerk [21], this variation may be described by

$$\phi(\overline{x_w}) = a + bexp(-c\overline{x_w})\cos\big(d\pi(\overline{x_w} - e)\big) + fexp(-g\overline{x_w}) \qquad (14)$$

where $\overline{x_w} = x_w/\overline{d_p}$ is the distance normal to the inner surface of the channel wall normalised by the average particle diameter, and a to g are constants whose values are given for the different bed-to-particle diameter ratios investigated here in Table S1 of the Supplementary Information.

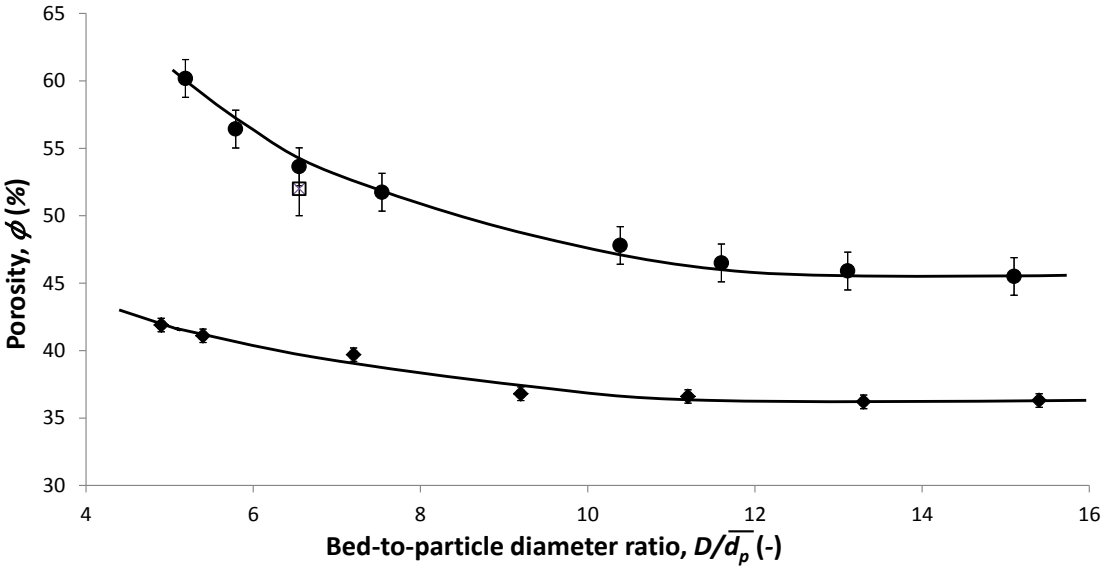

(a)

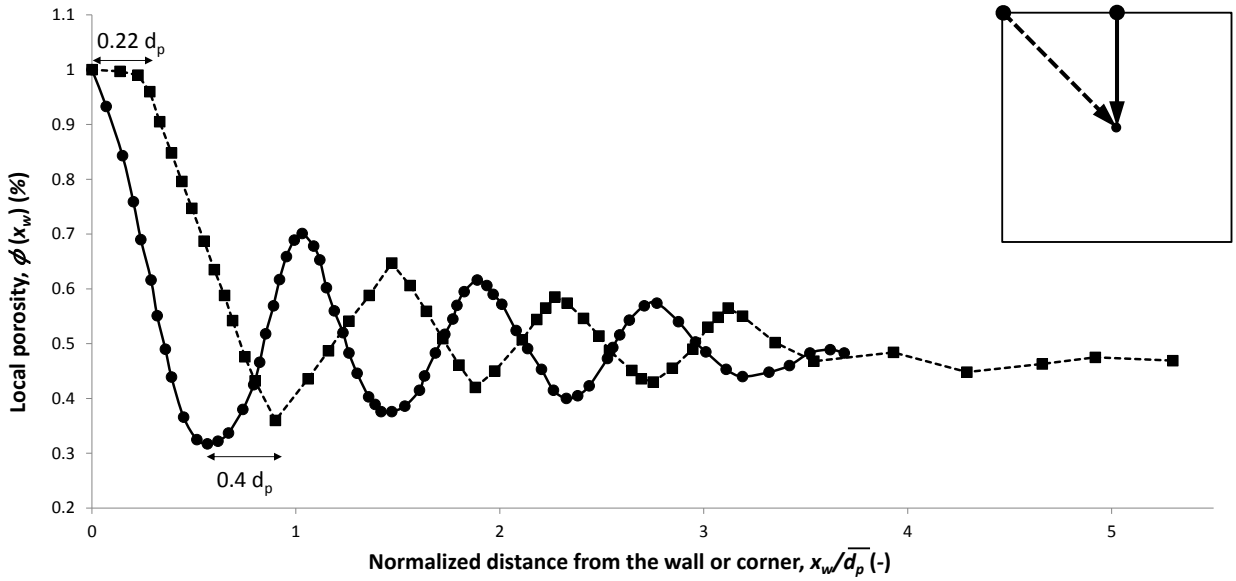

(b)

Figure 7. Porosity character of μPBs as derived from the models: (a) variation of porosity with the bed-to-particle diameter ratio (circles), and the direct measurement as described in Part A for the $D/\overline{d_p} = 6.6$ μPB (open square) and data obtained by De Klerk [21] for a macroscale packed beds of cylindrical cross-section (diamonds); and (b) example variation of porosity with normal distance from the wall (solid line) and diagonal distance from the corner (broken line) for $D/\overline{d_p}$=7.54 (similar data for all the other μPBs are provided in the SI). The lines are a guide for the eye only.

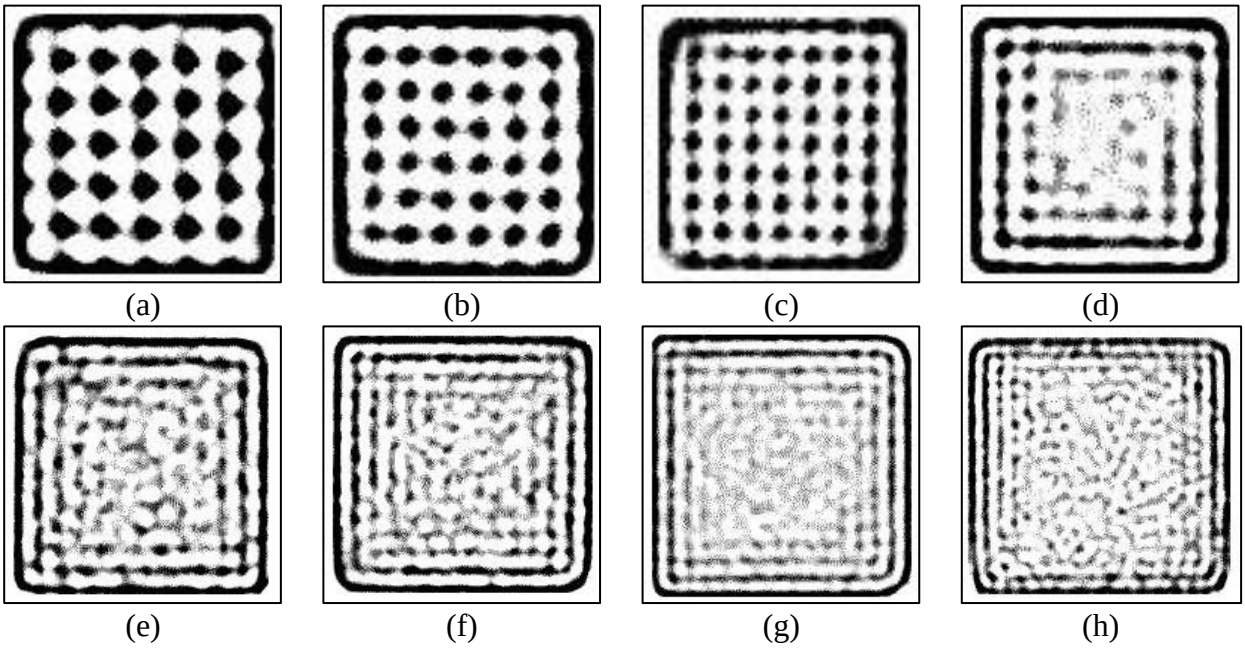

Figure 8. Solid density maps obtained by averaging over the X-ray microtomography images along the length of the μPBs for $D/\overline{d_p}$ equal to: (a) 5.2; (b) 5.8; (c) 6.6; (d) 7.5; (e) 10.4; (f) 11.6; (g) 13.1 and (h) 15.1.

The contacts between particles in a packed bed can be joined to form a network [22]. These networks are characterised by a mean coordination number, $\overline{Z}$, which represents the average number of contacts experienced by the particles in the bed. Figure 9(a) shows that this coordination number increases with the bed-to-particle diameter ratio in an initially non-linear manner up to a diameter ratio of around 8 before it continues to rise in what appears to be a linear manner. The mean coordination number of the μPBs whose diameter ratio exceeds around 10 take on values commensurate with those associated with random packings of monodisperse spheres, which fall between 5.5 for 'loose packings' through to around 6.5 for 'close packings' [23]. It is not clear from the data available here if the mean coordination number will pass beyond this limit, but this may well occur due to the dispersity in the particle size.

This increasing trend with bed-to-particle diameter ratio can be understood by considering Figure 9(b), which shows the variation of the local mean coordination number with normal distance from the wall for the various μPBs considered here along with the fit to the following functional form,

$$\bar{Z}(\overline{x_w}) = Aexp(-B\overline{x_w}) + C \qquad (15)$$

where *A*, *B* and *C* are constants whose values are given for the different bed-to-particle diameter ratios investigated here in Table S2 in the Supplementary Information. Clearly the mean coordination

number increases from a minimum at the wall – as expected due to the presence of the wall on the outside of the outermost layer of particles – until it reaches a plateau in the bulk of the bed. Thus, the increasing trend seen in Figure 9(a) *in part* has its origins in the increasing influence the bulk of the bed has on the mean coordination number as the bed size increases relative to the particle size. The change-down in the slope seen at $D/\overline{d_p} \approx 6$ reflects the plateau in the local coordination number occurs at $x_w/\overline{d_p} > 3$. Figure 9(b) also reveals that the mean coordination number at a given normalised distance from the wall also increases with bed-to-particle diameter ratio. This clearly suggests that there is a second origin of the increasing trend see in Figure 9(a) beyond the volumetric one. As the values of the local mean coordination number in the bulk of the bed appear to fall between the 'loose packing' and 'close packing' limits, this suggests the degree of packing achieved in the beds investigated here increases with the bed-to-particle diameter ratio.

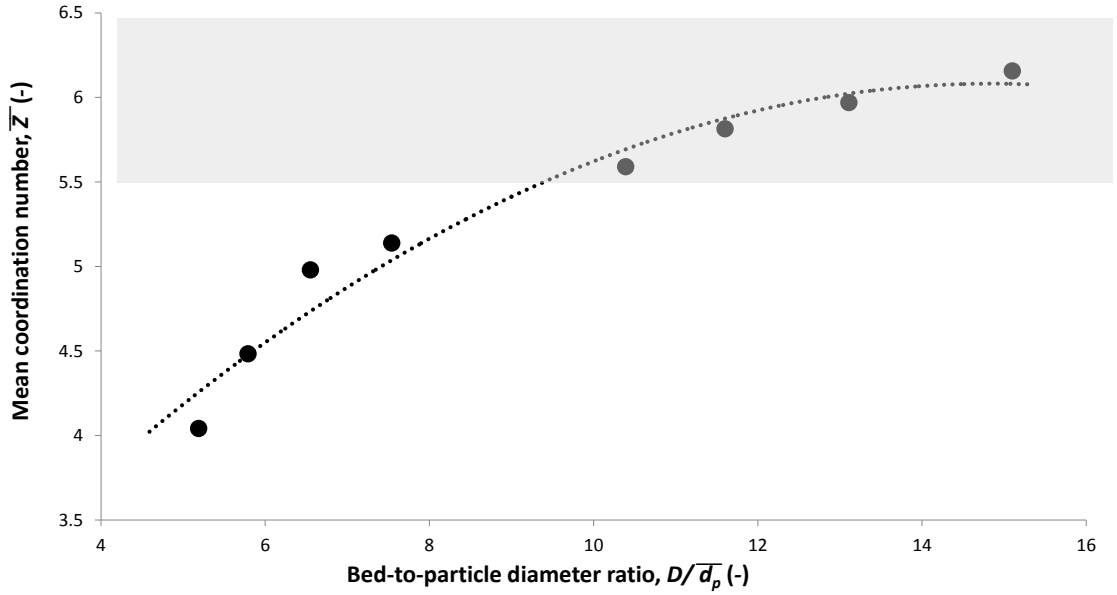

(a)

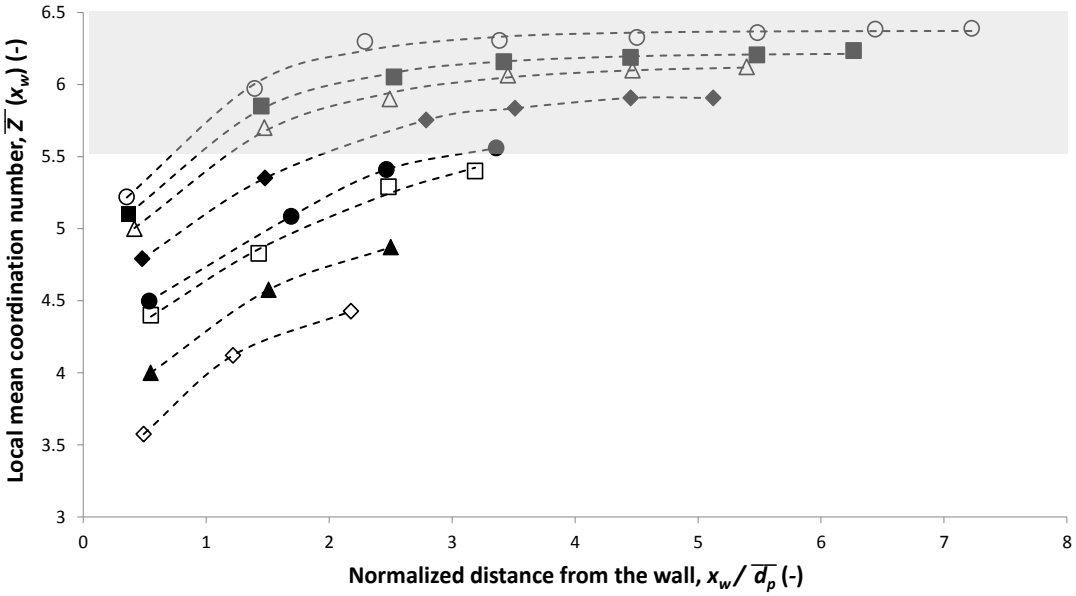

(b)

Figure 9. Coordination number variation with: (a) bed-to-particle diameter ratio; and (b) normalized distance from the bed wall for $D/\overline{d_p}$ =5.2 (open diamonds); 5.8 (solid triangles); 6.6 (open squares); 7.5 (solid circles); 10.4 (solid diamonds); 11.6 (open triangles); 13.1 (solid squares) and 15.1 (open circles). The lines are a best fit expressed as functional form in Equation (15).

5. Conclusions

In Part A [11], we reported a new method that derives models of micro-packed beds (μPBs) of near-spherical particles from X-ray microtomography grayscale images of limited resolution compared to the characteristics dimensions of the particles and porosity. The new method is distinguished by it not requiring a grayscale threshold to partition the images into solid and void phases, and its retention of the underlying spherical geometry, two issues that are particularly problematic when more traditional approaches are used to build models of μPBs. Whilst the models obtained from the new method provide a far better basis for estimating the porosity of μPBs, they contain defects in the form of particles that overlap each other and the bed wall, and which do not contact any other sphere ('suspended particles'). It is shown here that a reverse Monte Carlo (RMC) algorithm combined with simulated annealing (SA) can eliminate these defects by addressing the two major issues in the approach taken in Part A: (1) shifting from a single particle size (equal to the mean) to the experimentally identified particle size distribution; and (2) refining the particle positions within constraints defined by the uncertainty in their initial determination.

A μPB model obtained *via* application of RMC-SA to an initial model built using the approach in Part A yielded a porosity that was consistent with its directly determined counterpart. This approach

also yielded a variation of porosity with bed-to-particle diameter ratio that was consistent with this experimental data and, allowing for different bed cross-sections (square *vs.* circular) data published elsewhere. The porosity was found to be near unity at the wall of the μPBs and to vary in an oscillatory manner normal to it for up to three particle diameters into the bed. The mean coordination number was also found to vary over the same distance from the bed wall where it was a minimum. The values of the mean coordination number in the bulk of the bed fell between that associated with 'loose random packings', which occurred for the bed of the smallest bed-to-particle diameter ratio, to 'close packings' in the largest beds relative to the particles. These observations suggest there are two origins for the variation in the mean coordination number with bed-to-particle size ratio: a volumetric one in which the bulk value exerts increasing influence as the ratio increases, and the degree of packing, where this too increases with the size ratio.

Acknowledgement

The X-ray micro-computed tomography was undertaken at Adelaide Microscopy, a node of the Australian Microscopy & Microanalysis Research Facility (AMMRF). A part of code implemented for this research was run on the computational facilities in the eResearch SA organization. Also, MNK and HE acknowledge the University of Adelaide for their IPRS, APA and ASA PhD scholarships.

Nomenclature

Latin letters

a	Coefficient of correlation describing the variation of porosity of μPB with normal distance from the wall (Equation 14) [dimensionless]
A	Coefficient of correlation describing the variation of local mean coordination number with normal distance from the wall (Equation 15) [dimensionless]
b	Coefficient of correlation describing the variation of porosity of μPB with normal distance from the wall (Equation 14) [dimensionless]
B	Coefficient of correlation describing the variation of local mean coordination number with normal distance from the wall (Equation 15) [dimensionless]
c	Coefficient of correlation describing the variation of porosity of μPB with normal distance from the wall (Equation 14) [dimensionless]
C	Coefficient of correlation describing the variation of local mean coordination number with normal distance from the wall (Equation 15) [dimensionless]
d	Coefficient of correlation describing the variation of porosity of μPB with normal distance from the wall (Equation 14) [dimensionless]
d_i	Radius of particle i
d_{ij}	Minimum distance between particles that may exist in a μPB [m]

d_{iw}	Minimum distance between the particle and wall in the absence of an overlap that may exist in a μPB [m]
d_p	Particle size [m]
$\overline{d_p}$	Average particle diameter [m]
D	Micro-capillary size [m]
D_{ij}	Overlap between particle *i* and particle *j* [m]
D_{iw}	Overlap between particle *i* and wall of bed [m]
D_{i0}	Amount the displacement of the particle from its initial position exceeds the uncertainty associated with the initial centroid position of the particle *i* [m]
$D/\overline{d_p}$	Bed-to-particle diameter ratio [dimensionless]
e	Coefficient of correlation describing the variation of porosity of μPB with normal distance from the wall (Equation 14) [dimensionless]
f	Coefficient of correlation describing the variation of porosity of μPB with normal distance from the wall (Equation 14) [dimensionless]
F	Objective function [dimensionless]
g	Coefficient of correlation describing the variation of porosity of μPB with normal distance from the wall (Equation 14) [dimensionless]
$\hat{\mathbf{n}}_w$	Unit normal to the wall-*w* [dimensionless]
P	Probability [dimensionless]
p_w	Distance from the origin [dimensionless]
T	Temperature [K]
W	Associated weight to the sub-functions [dimensionless]
$\mathbf{x}$	Distance vector defining the centroids of a particle relative to an origin [m]
$\mathbf{x}_{i0}$	Position of the particle in the initial 3D structure obtained from the method described in Part A [m]
x_w	Distance from the wall/corner of μPB [m]
$\overline{x_w}$	Normalized distance from the wall/corner of μPB [dimensionless]
$\overline{Z}(x_w)$	Local mean coordination number [dimensionless]
$\overline{Z}$	Mean coordination number [dimensionless]

Greek letters

α	Weight parameter [dimensionless]
β	Weight parameter [dimensionless]
ξ	Corresponding random parameter to the changing the size of the particle, selected in a uniform way from the range [0,1) [dimensionless]
ξ_α	Corresponding random parameter to the displacing the position of the sphere, selected in a uniform way from the range [0,1) [dimensionless]
δ	Dirac delta function [dimensionless]
δd	Amount of change in the size of particle [m]
δd_{max}	Maximum possible change allowed in the diameter of particle [m]
δx_α	Amount of displacement in the position of the sphere in the α-coordinate directions [m]
$\delta x_{\alpha,max}$	Maximum possible displacement allowed in the α-coordinate direction [m]

σ	Standard deviation [m]
σ_i	Standard deviation associated with the position of the particle in the initial 3D structure obtained from the method described in Part A [m]
ϕ	Local porosity [%]
μ	Mean [m]
κ	Skewness [dimensionless]
ΔF	Change in objective function [dimensionless]

Subscripts

e	Refer to the values from experiment
m	Refer to the values from model
pp	Particle-particle
pw	Particle-wall
p	Particle centroids
s	Size distribution of particle
i, j	SPH particle index

Abbreviations

PSD	Particle Size Distribution
RMC	Reverse Monte Carlo
SA	Simulated Annealing
SPH	Smoothed Particle Hydrodynamics
μPB	Micro-packed bed
μTAS	Micro Total-Analysis-System

References

1. Reyes, D.R., et al., *Micro total analysis systems. 1. Introduction, theory, and technology.* Analytical chemistry, 2002. **74**(12): p. 2623-2636.
2. Auroux, P.-A., et al., *Micro total analysis systems. 2. Analytical standard operations and applications.* Analytical chemistry, 2002. **74**(12): p. 2637-2652.
3. Erickson, D. and D. Li, *Integrated microfluidic devices.* Analytica Chimica Acta, 2004. **507**(1): p. 11-26.
4. Hu, G. and D. Li, *Multiscale phenomena in microfluidics and nanofluidics.* Chemical Engineering Science, 2007. **62**(13): p. 3443-3454.
5. Van den Berg, A. and T. Lammerink, *Micro total analysis systems: microfluidic aspects, integration concept and applications,* in *microsystem technology in chemistry and life science*. 1998, Springer. p. 21-49.
6. Harmsen, G.J., *Reactive distillation: The front-runner of industrial process intensification: A full review of commercial applications, research, scale-up, design and operation.* Chemical Engineering and Processing: Process Intensification, 2007. **46**(9): p. 774-780.

7. Burns, J.R., J.N. Jamil, and C. Ramshaw, *Process intensification: operating characteristics of rotating packed beds — determination of liquid hold-up for a high-voidage structured packing.* Chemical Engineering Science, 2000. **55**(13): p. 2401-2415.

8. Van Gerven, T. and A. Stankiewicz, *Structure, energy, synergy, time. The fundamentals of process intensification.* Industrial & Engineering Chemistry Research, 2009. **48**(5): p. 2465-2474.

9. Kockmann, N., *Transport phenomena in micro process engineering*. 2007: Springer Science & Business Media.

10. Aggarwal, P., H.D. Tolley, and M.L. Lee, *Monolithic bed structure for capillary liquid chromatography.* Journal of Chromatography A, 2012. **1219**(0): p. 1-14.

11. Navvab Kashani, M., et al., *A new method for reconstruction of the structure of micro-packed beds of spherical particles from desktop X-ray microtomography images. Part A. Initial structure generation and porosity determination.* Chemical Engineering Science, 2016. **146**: p. 337-345.

12. Otsu, N., *A threshold selection method from gray-level histograms.* Systems, Man and Cybernetics, IEEE Transactions on, 1979. **9**(1): p. 62-66.

13. McGreevy, R.L., *Reverse Monte Carlo modelling.* Journal of Physics: Condensed Matter, 2001. **13**(46): p. R877.

14. Kirkpatrick, S., D.G. Jr., and M.P. Vecchi, *Optimization by simmulated annealing.* Science, 1983. **220**(4598): p. 671-680.

15. Georgalli, G.A. and M.A. Reuter, *A particle packing algorithm for pellet design with a predetermined size distribution.* Powder Technology, 2007. **173**(3): p. 189-199.

16. Caramia, M. and P. Dell'Olmo, *Multi-objective management in freight logistics: Increasing capacity, service level and safety with optimization algorithms*. 2008: Springer Science & Business Media.

17. Dersoir, B., *Clogging in micro-channels: from colloidal particle to clog*, 2015, Université Rennes 1.

18. Mays, D.C. and J.R. Hunt, *Hydrodynamic aspects of particle clogging in porous media.* Environmental science & technology, 2005. **39**(2): p. 577-584.

19. Zivkovic, V. and M. Biggs, *On importance of surface forces in a microfluidic fluidized bed.* Chemical Engineering Science, 2015. **126**: p. 143-149.

20. Biggs, M., et al., *Importance of surface forces in a micro-fluidized bed.* Chemeca 2012: Quality of life through chemical engineering: 23-26 September 2012, Wellington, New Zealand, 2012: p. 698.

21. de Klerk, A., *Voidage variation in packed beds at small column to particle diameter ratio.* AIChE Journal, 2003. **49**(8): p. 2022-2029.

22. Torquato, S., *Random heterogeneous materials: microstructure and macroscopic properties*. Vol. 16. 2002: Springer Science & Business Media.

23. Bernal, J.D. and J. Mason, *Packing of spheres: co-ordination of randomly packed spheres.* Nature, 1960. **188**(4754): p. 910-911.

Supplementary information

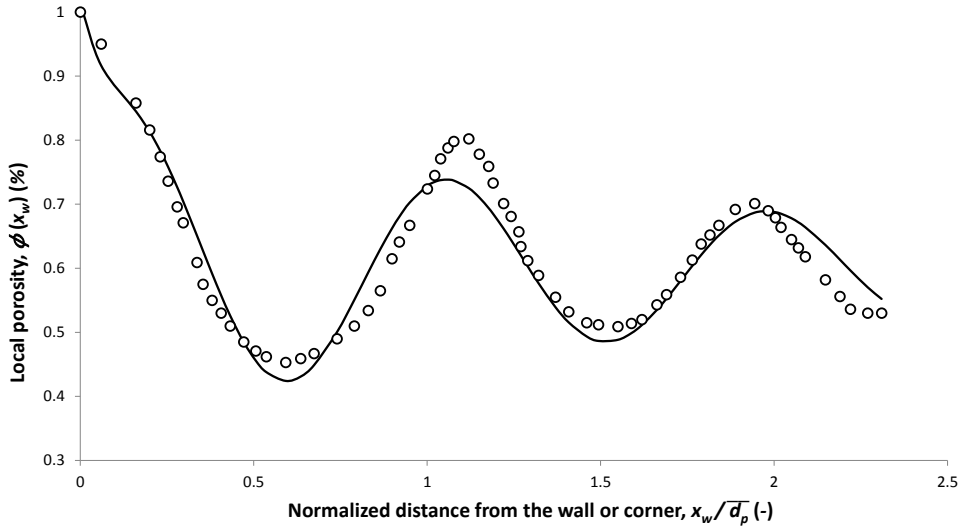

(a)

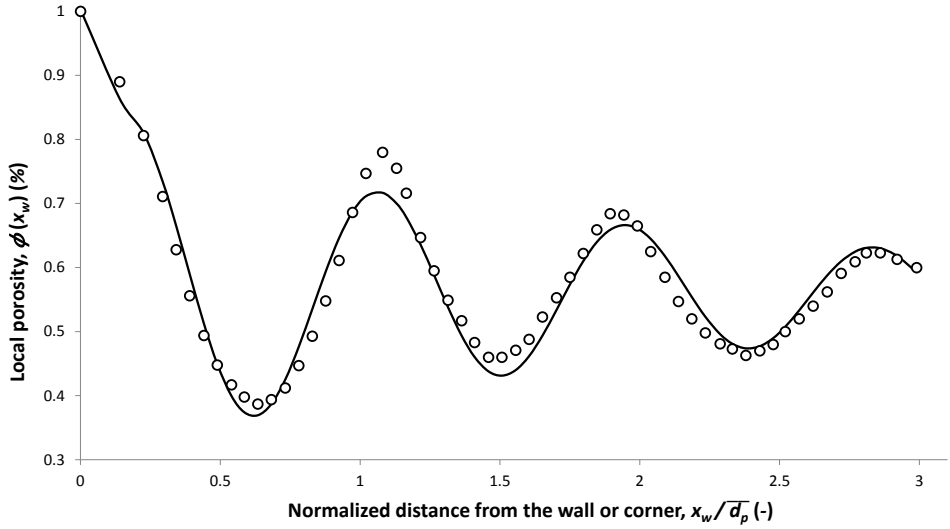

(b)

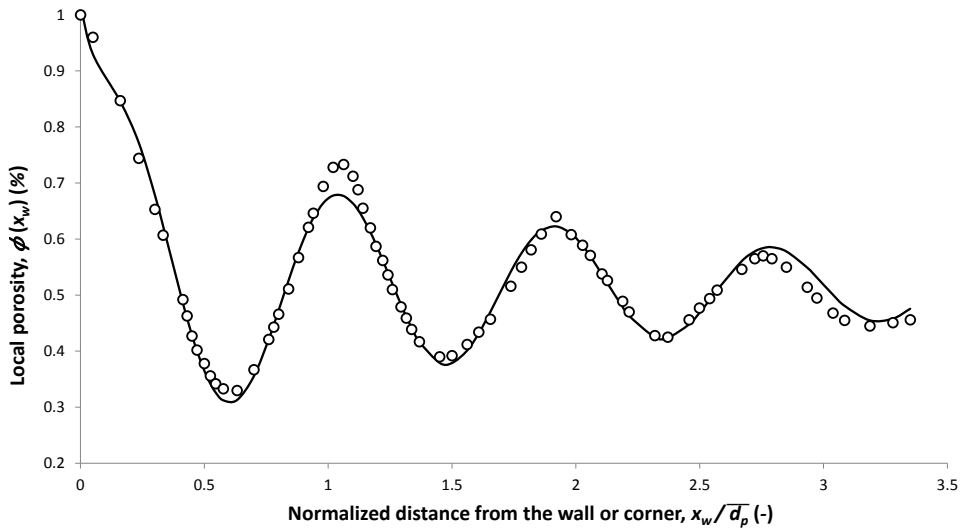
Local porosity, $\phi(x_w)$ (%)
Normalized distance from the wall or corner, $x_w/\overline{d_p}$ (-)

(c)

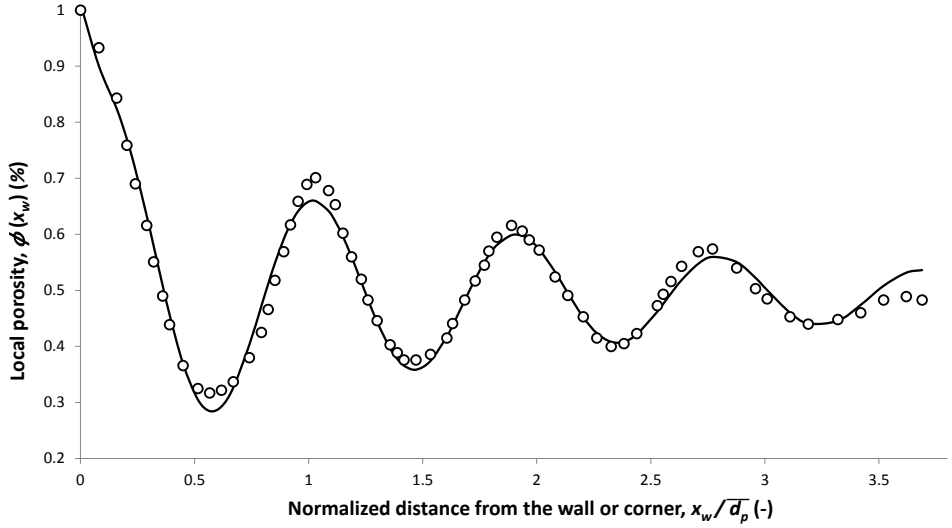
Local porosity, $\phi(x_w)$ (%)
Normalized distance from the wall or corner, $x_w/\overline{d_p}$ (-)

(d)

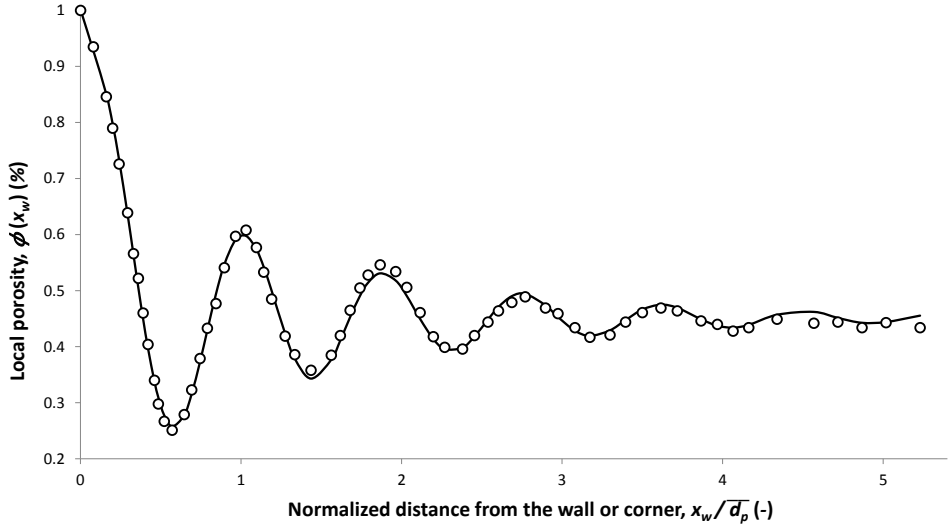
Local porosity, $\phi(x_w)$ (%)
Normalized distance from the wall or corner, $x_w/\overline{d_p}$ (-)

(e)

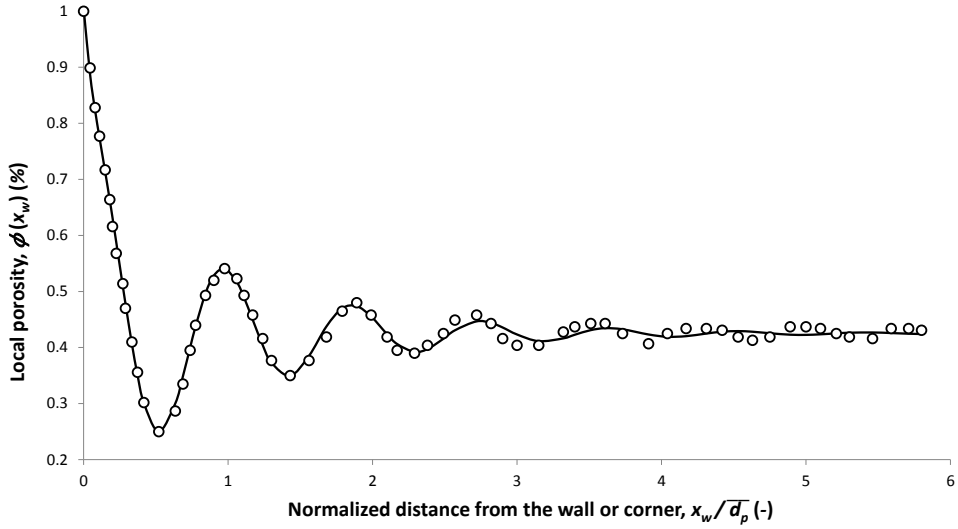
Local porosity, $\phi(x_w)$ (%)
Normalized distance from the wall or corner, $x_w/\overline{d_p}$ (-)

(f)

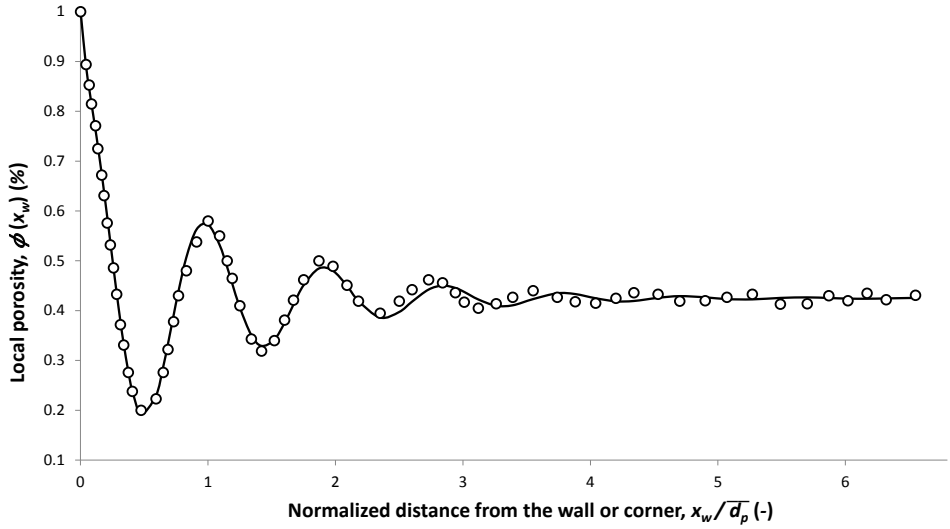
Local porosity, $\phi(x_w)$ (%)
Normalized distance from the wall or corner, $x_w/\overline{d_p}$ (-)

(g)

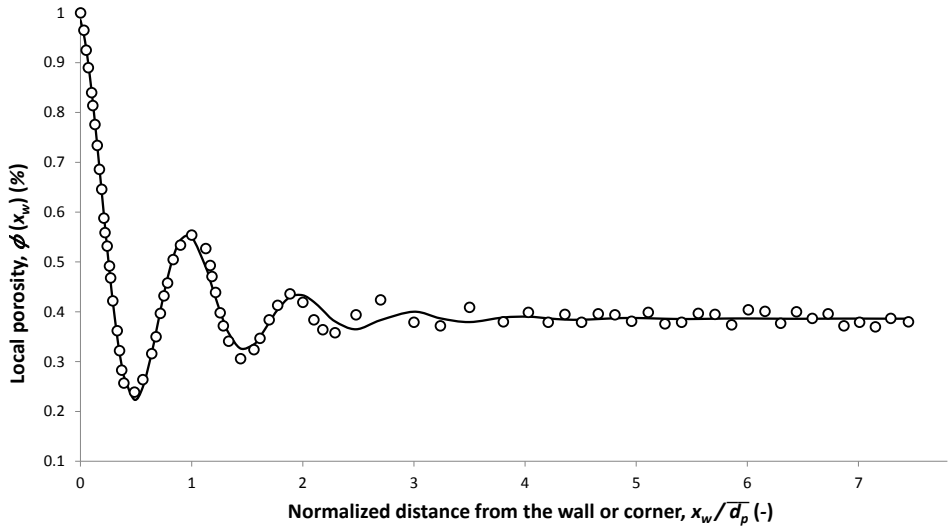

(h)

Figure S1. Variation of local porosity with normal distance from the wall, derived from the models (open circles) and functional form of Equation 14 (solid line), for bed-to-particle diameter ratio of: (a) 5.2; (b) 5.8; (c) 6.6; (d) 7.5; (e) 10.4; (f) 11.6; (g) 13.1 and (h) 15.1.

Table S1. Coefficients of correlation in Equation (14), which describes the variation of porosity with normal distance from the wall of μPBs of different bed-to-particle size ratios, $D/\overline{d_p}$

$D/\overline{d_p}$	*a*	*b*	*c*	*d*	*E*	*f*	*g*	R^2	*RMSE*
5.2	0.5982	-0.231	0.470	2.170	0.604	0.285	13.230	0.917	0.035
5.8	0.560	-0.255	0.450	2.260	0.628	0.379	11.420	0.959	0.026
6.6	0.512	-0.273	0.472	2.290	0.612	0.418	10.200	0.980	0.019
7.5	0.492	-0.280	0.503	2.252	0.586	0.369	10.060	0.976	0.021
10.4	0.451	-0.302	0.703	2.302	0.592	0.423	7.370	0.996	0.010
11.6	0.425	-0.289	0.940	2.250	0.540	0.356	12.520	0.994	0.010
13.1	0.425	-0.384	0.952	2.133	0.523	0.218	18.410	0.994	0.012
15.1	0.386	-0.422	1.160	2.009	0.501	0.178	1.737	0.992	0.015

Table S2. Constants of the correlation in Equation (15), which describes the variation of the local mean coordination number with normal distance from the wall of μPBs of different bed-to-particle size ratios, $D/\overline{d_p}$.

$D/\overline{d_p}$	*A*	*B*	*C*	R^2	*RMSE*
5.2	-1.719	1.034	4.608	1.000	-
5.8	-1.715	0.720	5.155	1.000	-
6.6	-1.982	0.396	5.984	0.994	0.061
7.5	-1.892	0.475	5.959	0.997	0.048
10.4	-1.655	0.680	5.979	0.998	0.024
11.6	-1.611	0.852	6.134	0.997	0.029
13.1	-1.595	0.977	6.216	0.998	0.022
15.1	-1.707	1.100	6.372	0.994	0.038